Novel inductively coupled ear-bars (ICEs) to enhance restored fMRI signal from susceptibility compensation in rats

Yi Chen[1,2], Zachary Fernandez[2,3], Norman Scheel[2], Mahsa Gifani[4], David C. Zhu[2,3], Scott E. Counts [3,4,5,6,7], Anne M. Dorrance[3,8],

Daniel Razansky[9,10,11], Xin Yu [12], Wei Qian[13], Chunqi Qian[2,13,*]

[1]Department of High-field Magnetic Resonance, Max Planck Institute for Biological Cybernetics, Tuebingen 72076, Germany,
[2]Department of Radiology and Cognitive Imaging Research Center, Michigan State University, East Lansing, MI 48824, United States,
[3]Neuroscience Program, Michigan State University, East Lansing, MI 48824, United States,
[4]Department of Translational Neuroscience, Michigan State University, Grand Rapids, MI 49503, United States,
[5]Department of Family Medicine, Michigan State University, Grand Rapids, MI 49503, United States,
[6]Department of Hauenstein Neurosciences Center, Mercy Health Saint Mary's Hospital, Grand Rapids, MI 49508, United States,
[7]Michigan Alzheimer's Disease Research Center, Ann Arbor, MI 48105, United States,
[8]Department of Pharmacology and Toxicology, Michigan State University, East Lansing, MI 48824, United States,
[9]Institute of Pharmacology and Toxicology and Institute for Biomedical Engineering, Faculty of Medicine, University of Zurich, Zurich 8006, Switzerland,
[10]Department of Information Technology and Electrical Engineering, ETH Zurich, Institute for Biomedical Engineering, , Zurich 8092, Switzerland,
[11]Zurich Neuroscience Center, Zurich 8057, Switzerland,
[12]Martinos Center for Biomedical Imaging, Massachusetts General Hospital and Harvard Medical School, Charlestown, MA 02114, United States,
[13]Department of Electrical and Computer Engineering, Michigan State University, East Lansing, MI 48824, United States

*Corresponding author: Department of Radiology and Cognitive Imaging Research Center, Michigan State University, East Lansing, MI, 48824, United States.
Email: qianchu1@msu.edu

Functional magnetic resonance imaging faces inherent challenges when applied to deep-brain areas in rodents, e.g. entorhinal cortex, due to the signal loss near the ear cavities induced by susceptibility artifacts and reduced sensitivity induced by the long distance from the surface array coil. Given the pivotal roles of deep brain regions in various diseases, optimized imaging techniques are needed. To mitigate susceptibility-induced signal losses, we introduced baby cream into the middle ear. To enhance the detection sensitivity of deep brain regions, we implemented inductively coupled ear-bars, resulting in approximately a 2-fold increase in sensitivity in entorhinal cortex. Notably, the inductively coupled ear-bar can be seamlessly integrated as an add-on device, without necessitating modifications to the scanner interface. To underscore the versatility of inductively coupled ear-bars, we conducted echo-planner imaging-based task functional magnetic resonance imaging in rats modeling Alzheimer's disease. As a proof of concept, we also demonstrated resting-state-functional magnetic resonance imaging connectivity maps originating from the left entorhinal cortex—a central hub for memory and navigation networks-to amygdala hippocampal area, Insular Cortex, Prelimbic Systems, Cingulate Cortex, Secondary Visual Cortex, and Motor Cortex. This work demonstrates an optimized procedure for acquiring large-scale networks emanating from a previously challenging seed region by conventional magnetic resonance imaging detectors, thereby facilitating improved observation of functional magnetic resonance imaging outcomes.

Key words: susceptibility artifact; resting-state fMRI; inductive coils; entorhinal cortex; Alzheimer's disease.

Introduction

In magnetic resonance imaging (MRI) scanners, the surface coil and coil array could be placed near the rodent brains to have a good signal-to-noise ratio (SNR) for the brain parenchyma adjacent to the coil. However, the SNR decreases dramatically as the distance from the coil/coil array increases (Mahesh 2013). This issue is inevitable due to the decaying sensitivity profile of the surface coil/coil array, especially for rodent imaging inside high-field magnets where the confined bore space is largely occupied by the rodent holder, air supply tubing, heating pad, etc. To reduce hardware complexity and to boost sensitivity, inductively coupled detectors can be placed near the targeted region of interest (ROI) to wirelessly relay locally detected MR signals with the external

surface radiofrequency (RF) coil (Schnall et al. 1986; Wirth et al. 1993; Chen et al. 2022). In addition, sensitivity enhancement in regions near the targeted ROI can be maintained within a good range, as long as inductive coupling remains larger than transmission loss (Chen et al. 2022). Conventionally, the teeth and ears of the rodents in the rodent holder were secured by a bite bar and ear bars, respectively (Lee et al. 2010; Chen et al. 2020), in an MRI-compatible stereotaxic frame. Therefore, it is particularly practical and feasible to combine the ear bars with inductively coupled detectors, to enhance the detection sensitivity, especially in deep-brain regions, e.g. the amygdala (Hernandez et al. 2019) and entorhinal cortex (EC), owing to their unique locations in the rodent brain (Khan et al. 2014) that are closer to the ear bars.

In addition, magnetic susceptibility artifacts are prevalent on the boundary of air-containing ear cavities in rodents (Lee et al. 2019; Lee et al. 2022). Although efforts have been made to reduce susceptibility artifacts (Mandeville et al. 1998; Li et al. 2015; Yoo et al. 2020; Ryu et al. 2021), these efforts are mostly focused on restoring lost signals in echo-planar imaging (EPI)-based blood oxygen level-dependent (BOLD) functional magnetic resonance imaging (fMRI) images over large scales across the entire brain. It remains challenging to enable true whole-brain fMRI imaging. The fMRI image signal loss at the location of EC is due to its proximity to the air-tissue interface in the ears, which introduces a high level of magnetic field inhomogeneity. While the higher magnetic field strength could offer higher signal sensitivity, it also exacerbates the problem of susceptibility artifacts (Farahani et al. 1990). To the best of our knowledge, there is no report on the use of standard current shims to address the pointillistic character of homogeneity distortion of magnetic field near the middle ear of rat brain. Several studies have already been done to reduce susceptibility artifacts. An equal-TE ultrafast 3D gradient-echo imaging method was developed to provide high tolerance to magnetic susceptibility artifacts in rat cortex with optical fiber implantation at 9.4T (Ryu et al. 2021). The middle ear filled with air is separated from the external ear by the tympanic membrane (Li et al. 2015). When this membrane was penetrated, Fomblin Y (Li et al. 2015) or toothpaste (Mandeville et al. 1998) could fill the ear cavities to replace the air thus restoring susceptibility-induced MRI signal dropout. However, these methods to reduce distortion and to restore signal dropout in deep brain regions in proximity to the ear cavities were unsatisfactory because the fluidic Fomblin Y could not be kept in the cavities, the toothpaste is skin-irritating, and the implementation procedure needs specific expertise. Therefore, it is highly desirable to have a simple, skin-friendly strategy without modification of the MRI interface to restore signal dropout in deep-brain regions of rodents, including EC and amygdala (Hernandez et al. 2019). This will allow a true whole-brain imaging scheme to provide a comprehensive understanding of brain networks and function.

The EC is the interface between the hippocampus and neocortex (Fyhn et al. 2004; Brun et al. 2008), which together form a widespread network hub for memory, navigation, and the perception of time (Witter and Moser 2006; Brun et al. 2008; Tsao et al. 2018). It is a potential target of deep-brain stimulation (DBS) in Alzheimer's disease (AD) patients and animal models of dementia; however, the mechanism for DBS remains unclear. Studies have revealed that DBS of the EC area enhanced memory (Suthana et al. 2012; Jacobs et al. 2016; Mankin and Fried 2020) in humans. This is highly consistent with the observation in AD rodent models (Xia et al. 2017), which provides a platform for mechanistic studies, combining imaging methods with cell-specific optogenetic stimulation (Zhang et al. 2013; Lu et al. 2016; Chavoshinezhad et al. 2021; Salvan et al. 2021; Tsoi et al. 2022). fMRI, especially, resting-state fMRI (rs-fMRI; Biswal et al. 1995), is a useful method to noninvasively study brain-wide dynamics (Logothetis 2008) and to provide translational knowledge between humans and animal models. rs-fMRI has been widely used in both healthy human subjects and patients and multiple animal species with various neurosurgical and psychiatric disorders (Lv et al. 2018), e.g. AD. For instance, despite observed abnormalities in the default-mode network (DMN) early in AD (Schwindt et al. 2013; Zhu et al. 2013; Grieder et al. 2018), the role of EC function/dysfunction within the DMN and its contributions to associated network abnormalities in AD are far less explored due to the location of EC in the brain, i.e.

one of the deepest regions in close proximity to air-containing ear cavities.

Hence, as a proof-of-concept demonstration, we present an animal fMRI strategy to restore EPI signal loss adjacent to ear cavities and to improve MR detection sensitivity of deep brain regions, particularly in EC, by ICE (Inductively Coupled Ear bars) combined with ear canal injection of baby cream. As an in vivo benchmark application of ICE in contrast to conventional surface coil arrays, we have embedded the ICE to show a nearly 2-fold enhancement of SNR in lateral EC. We evaluated this setup first by using task fMRI with electrical stimulation on the forepaw followed by rs-fMRI. In the task fMRI, we observed a robust evoked BOLD signal in the primary somatosensory cortex of forelimb (S1FL). In the rs-fMRI, we observed a robust DMN. Finally, we analyzed the seed-based rs-fMRI connectivity maps based on the left EC.

Material and methods
Flexible inductively coupled ear bars design, fabrication, and in vitro validation

Inside an MRI scanner, the rat head is secured by a bite bar from the rostral side and two ear bars from the lateral sides, leaving its dorsal side accessible by surface coils that are more effective for the upper half of the brain. Because of the geometrical constraint imposed by the ear-fixing apparatus, the surface coil should have a diameter smaller than the head width, creating a horizontal B_1 field across the edge of the surface coil (Fig. 1a). To enhance detection sensitivity in this region that corresponds to the lateral side in the lower half of the brain, an inductively coupled resonator was integrated with the ear bar to replace the conventional ear bars to stabilize the head during scanning. When the inductively coupled ear-bar is perpendicularly overlapping with the edge of the receiver coil, the ICE has a normal axis that is parallel to the B_1 field of the surface coil, thus creating effective inductive coupling. The ear bar was 3D-printed to have a 9-mm flange and a 2-mm shaft. The shaft was 3 mm away from the center of the flange so that when the shaft was inserted into the ear cannel and fit inside a positioning hole on the cradle, the center of the flange could be aligned approximately with the EC region that was about 3 mm above the ear cannel. The flange had a 0.4-mm-wide groove around its peripheral edge to accommodate the ICE circuit. To estimate the coupling efficiency between the ICE and the surface coil, finite element analysis was performed by COMSOL (COMSOL Inc, Stockholm, Sweden). The ICE was modeled as a two-turn solenoid with a 9-mm diameter and a 0.5-mm pitch distance. The bridge capacitance was numerically adjusted to tune the resonance frequency to 300 MHz. The surface coil (for rat head) was modeled as a square loop with a 14.6-mm side length and was numerically tuned to 300 MHz by a bridge capacitor. When the ICE was aligned with the edge of the surface coil and had its normal axis separated from the surface coil by 10 mm (the approximate distance from the ear cavity to the top surface of the brain), the energy transfer efficiency was ∼74%, assuming both resonators have a reasonably large quality factor of ∼50. As another example, when the surface coil was modeled as a smaller square (for mouse head) with a 10-mm side length and separated from the ICE's normal axis by 10 mm, the energy transfer efficiency became 66%, which was still sufficient for focal signal enhancement.

To fabricate an ICE detector (Fig. 1a), we wrapped a 32-gauge enameled copper wire around the flange for two turns and self-connected the conductor leads via a zero-biased diode (BBY52,
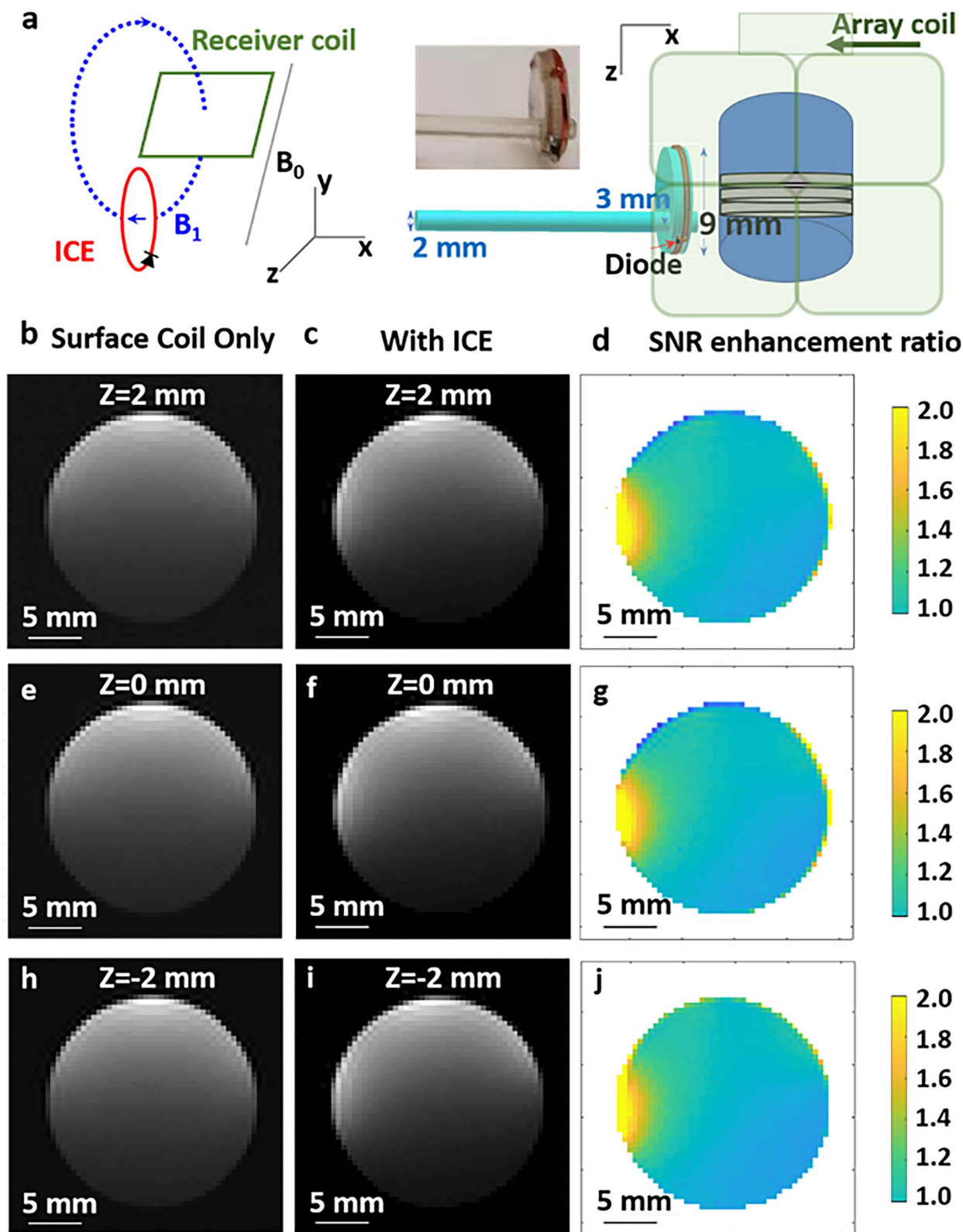
Fig. 1. Evaluation of inductive-coupled ear bars with EPI in phantoms. (a) The schematic diagram (left), the cartoon (right), and the real picture (middle) of an inductive coupler mounted on the flange of an ear bar for in vitro experimental setup. The ICE circuit consists of a loop inductor (labeled in red) connected in series with a zero-biased diode whose junction capacitance is utilized to resonate the circuit. The resonance frequency can be empirically adjusted by varying the turns and diameter of the loop inductor. Normally, more turns and larger diameters would lead to larger inductance and thus smaller resonance frequency. When the ICE plane is perpendicularly overlapping with the edge of the receiver coil (green), the ICE's normal axis is parallel to the B_1 field of the receiver coil, creating effective inductive coupling. (b–j) The left column is SNR maps obtained from Echo Planar Images acquired by the arrayed coil placed above the sample tube, based on the following parameters: TE = 20 ms, TR = 1 s, FOV = $26 \times 26 \times 16$ mm^3. The middle column is SNR maps acquired with an additional ICE pressed against the left wall of the sample tube, using the same acquisition parameters. The right column of the SNR enhancement ratio was obtained by dividing SNR maps in the middle column with SNR maps in the left column. (f) was acquired through the slice passing through the center axis of ICE, while (c) and (i) were acquired through the slices with 2-mm off-sets from the center position.
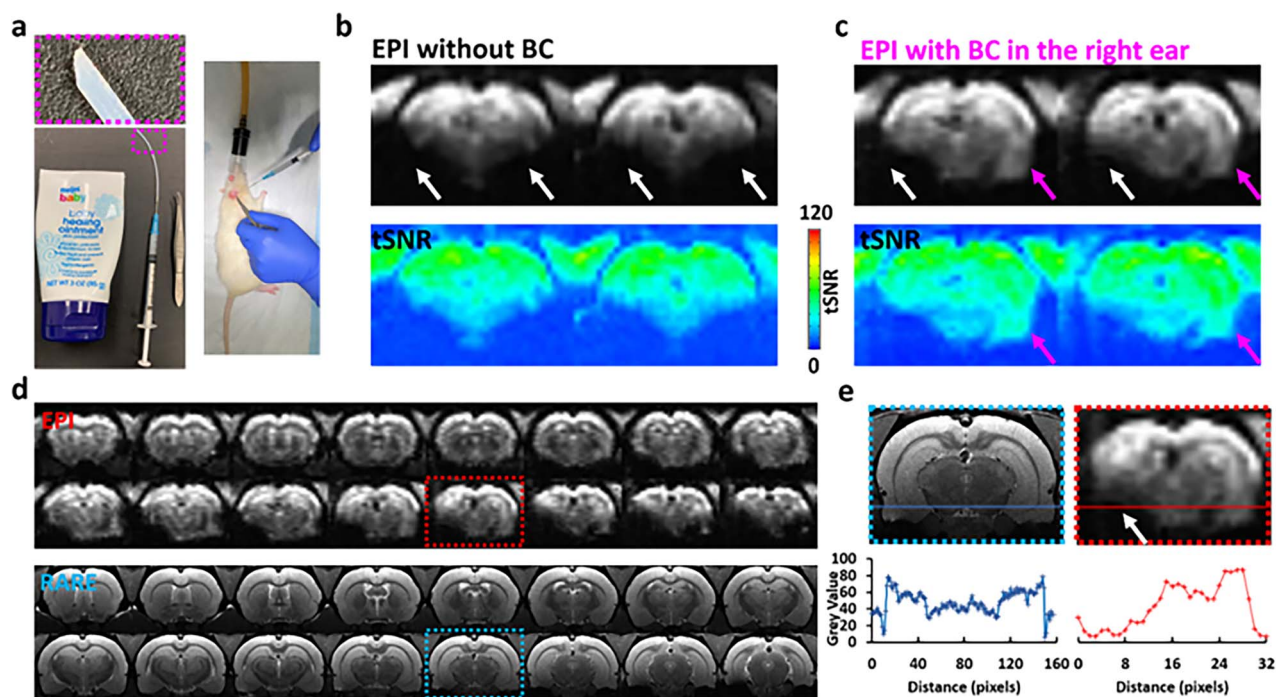
Fig. 2. Restored EPI signals in deep-brain regions with baby cream. (a) These pictures show the tip of the blunt tubing used to puncture the tympanic membrane and to introduce baby cream into the middle ear. (b) These pictures show representative EPI (upper row) and temporal signal-to-noise ratio (tSNR) maps (lower row) (voxel size = $0.5 \times 0.5 \times 0.5$ mm^3, TR = 1 s) without baby cream from a representative animal. White arrows demonstrate the susceptibility-induced EPI signal loss. (c) These pictures show representative EPI (upper row) and tSNR (lower row) (voxel size = $0.5 \times 0.5 \times 0.5$ mm^3, TR = 1 s) affected by the baby cream. Magenta arrows demonstrate the restored EPI signals in the right hemisphere with baby cream infusion in the right ear, while white arrows demonstrate the susceptibility-induced EPI signal loss in the left hemisphere. (d) These pictures show EPI (upper two rows) and RARE images (lower two rows) (pixel size = 0.1 mm × 0.1 mm, thickness 0.5 mm) from a representative animal with baby cream placed in the right ear and none in the left ear. (e) The image signal profile demonstrates the EPI signal restoration in the right hemisphere following baby cream injection, while the ear cavity has negligible influence on the image quality of RARE from a representative animal. The white arrow indicates the susceptibility artifacts.

Infenion, Neubiberg, Germany). During slice excitation pulses, the diode would be transiently turned on by the voltage induced across the inductor loop, thus detuning the ICE away from Larmor frequency. During MR signal acquisition, the junction capacitance of the diode provided the necessary capacitance to resonate the circuit around 301 MHz which was slightly above the Larmor frequency of a 7T scanner, based on the formula: $f = \frac{1}{2\pi\sqrt{LC}}$. When the ICE is approaching the rodent's lateral EC region via an ear bar, its edge perpendicularly overlaps with the edge of a receiver coil (or coil array) placed above the rodent's skull. As a result, the ICE's normal axis is parallel to the B_1 field of the receiver coil, creating effective inductive coupling, as demonstrated by the > 2-fold sensitivity gains in the SNR enhancement map (Fig. 1d, g, j). Owing to its proximity to the left lateral EC region, the ICE could sensitively detect regional signals and inductively relay these signals to the surface coil array placed on top of the brain (Fig. 2d, e).

Animals

All procedures in this study were conducted in accordance with guidelines set by the Institutional Animal Care and Use Committee of Michigan State University. We developed a rat model for mixed dementia by breeding the Tg344-19 rat model of AD (Cohen et al. 2013; Kelly et al. 2019) with the spontaneously hypertensive stroke-prone rat (SHRSP) model of cerebrovascular small vessel disease (Yamori et al. 1975; Pires et al. 2015). Tg344-19 AD rats express the human mutant APPswe and PS1Δ9 genes under the control of the mouse prion promoter (Cohen et al. 2013).

Hemizygous Tg344-19 rats were backcrossed onto the SHRSP genetic background, and the animals used in this study were the 10th generation of progeny. Transgene-positive (Tg+) animals were confirmed by PCR analysis of DNA extracted from ear punches. The present study used a total of nine Tg + or Tg- mixed dementia rats (four males, five females) (Kelly et al. 2019; Matin et al. 2021). All animals were three-in-one-housed in 12-12 hour on/off light–dark cycle conditions to assure undisturbed circadian rhythm and ad libitum access to chow and water.

Animal preparation for fMRI

Animals were first anesthetized with 5% isoflurane in a chamber and kept with 2% isoflurane with a nose cone during injection of baby cream (Fig. 2a shows the product photo, Dist. By Meijer Distribution, INC, Grand Rapids, MI, USA). The ingredients are 41% Petrolatum, and the rest are mineral oil, ceresin, lanolin alcohol, panthenol glycerin, and bisabolol. 0.1–0.2 mL baby cream was needed to fulfill each ear cavity to recover signal loss and reduce noise contamination. The detailed experimental procedure is demonstrated in Supplementary Movie 1. Subsequently, the animal was administered by an initial bolus of subcutaneous injection of dexmedetomidine (0.1 mg/kg, NDC 44567-600-04, WG Critical Care, USA). The isoflurane was then discontinued, and the animal was transferred to the scanner with dexmedetomidine (0.1 mg/kg/h) delivered subcutaneously. The animal's body temperature, arterial oxygen saturation level, and respiration rates were monitored and maintained within normal ranges when the animal was inside the scanner. Spontaneous respiration rate
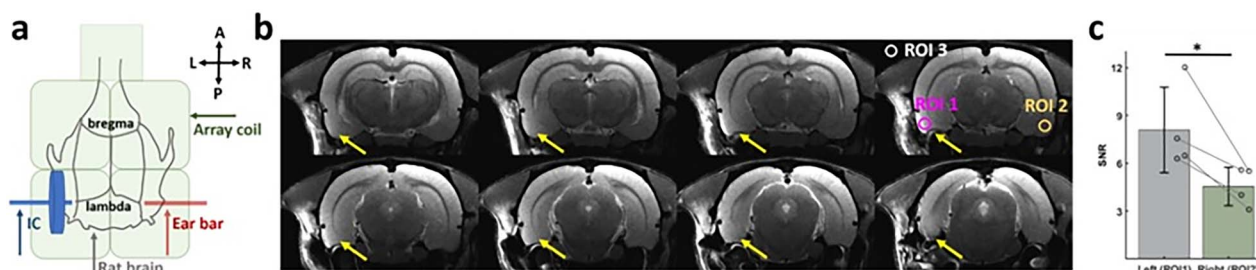
Fig. 3. ICE increased the SNR in EC. (a) 2D schematic of ICE placement (blue arrow) in contrast to standard ear bar (red arrow). (b) Example of RARE images with enhanced MRI signal due to ICE in the left hemisphere and without enhancement in the right hemisphere. (c) Significantly increased focal signal intensity in ROI 1 with the ICE placed on the left side compared to the signal intensity in ROI 2 where the right hemisphere has no ICE (*$P < 0.05$, paired samples t-test, $n = 4$ animals).

typically ranged from 50 to 70 breaths per minute during rs-fMRI image acquisition.

MRI acquisition

All images were acquired with a 7 T/16 cm aperture-bore small-animal scanner (Bruker BioSpin, Billerica, MA). A 72-mm quadrature volume coil and a ^{1}H receive-only 2×2 brain surface array coil (RF ARR 300 1H R. BR. 2×2 RO AD) were used to transmit and receive magnetic resonance signals, respectively. The console of the Bruker system adjusted the RF pulse attenuation automatically for individual rats.

Functional images (Fig. 2d, e) were acquired with a 2D gradient-echo EPI (GE-EPI) sequence with the following parameters: time of echo (TE) = 20 ms, time of repetition (TR) = 1 s, the field of view (FOV) = 2.6 cm × 2.6 cm × 1.6 cm, matrix size = 52 × 52 × 32, voxel size = 0.5 mm × 0.5 mm × 0.5 mm, flip angle: 90°, bandwidth: 333 kHz. Each rs-fMRI scan has the same parameters as the task fMRI and acquired 900 time points over 15 mis. We performed electrical stimulation on the left forepaw (5 Hz, 4 s, 333 μs width, 2 mA) (Fig. 3a) in blocks. Specifically, the block design paradigm included 10-s pre-stimulation, 4-s stimulation, and 11-s intervals, i.e. 15 s for each epoch and eight epochs for a full trial (2 m 10 s), as shown in Fig. S5(a).

We applied a higher resolution (100 μm) 2D RARE sequence to acquire 32 coronal slices with the same geometry as fMRI images, to accurately identify the left lateral EC in the coronal plane, with the following parameters: TR = 4200 ms, TE = 24 ms, Echo Spacing = 12 ms, FOV = 2.6 cm × 2.6 cm, matrix = 260 × 260, resolution = 100 μm × 100 μm, slice thickness = 0.5 mm, RARE factor = 4, and signal averaging = 2.

Immunohistochemistry

Post-fixed brain hemispheres were transferred to 15% sucrose in 0.1 M phosphate buffer until saturated, then 30% sucrose in 0.1 M phosphate buffer until saturated. Brains were frozen on dry ice and sectioned at a 40 μm thickness in a 1:12 series in the coronal plane using a freezing-sliding microtome (American Optical, Buffalo, NY). Serial sections were processed for immuno-histochemistry using the 6F/3D mouse monoclonal amyloid-beta antibody (1:50; ThermoFisher, Waltham, MA) to visualize amyloid plaque pathology.

Data analysis

All signal processing and analyses were implemented in MATLAB software (Mathworks, Natick, MA), FMRIB Software Library (FSL), and Analysis of Functional NeuroImages software (AFNI, NIH, USA). For evoked fMRI analysis of Fig. 2(d, e), Fig. S3, and S4, to generate BOLD functional maps, we applied pre-processing steps including motion correction, image registration, time course normalization, and averaged fMRI datasets from multiple trials for each animal. The regression analysis of the hemodynamic response function was based on the BLOCK function of the linear program 3dDeconvolve in AFNI. BLOCK (d, 1) computes a convolution of a square wave of duration d and makes a peak amplitude of block response = 1. To compute the evoked BOLD changes, ROI was defined based on the SIGMA Atlas: the right primary somatosensory area (Barriere et al. 2019).

For resting-state fMRI analysis (Fig. 4d, Fig. 5, and Fig. S6), the rs-fMRI processing pipelines using independent component analysis (ICA) and seed-based analyses are shown in Fig. S5(b). The pre-processing procedures followed those commonly used protocol in rat rs-fMRI data (spikes, motion-correction, slice-timing correction, and spatial blurring) (Nasrallah et al. 2016; Hsu et al. 2016a; Chuang et al. 2019; Liu et al. 2020; Pradier et al. 2021; Jung et al. 2022), including motion correction, despike, spatial blurring, and 0.001–0.1 Hz bandpass filtering in AFNI. Then we conducted the ICA analysis with 60 components using MELODIC in FSL to identify and remove non-neural artifacts (Griffanti et al. 2014; Griffanti et al. 2017). Previous rodent fMRI studies from different research groups used ICA proposed an IC number of 30 (Zerbi et al. 2015), 40 (Lu et al. 2012), and 50 (Liu et al. 2020), and even up to 100 (Mechling et al. 2016) for mice connectome. In this study, to separate noise components from detailed regions without splitting functionally connected networks, we used 60 components. With the references from FSL (Griffanti et al. 2014; Griffanti et al. 2017), we classified the IC component manually as a noise component if it included the following features: spatially, it is located predominantly at ventricles, brain boundaries, or white matters; spectrally, the frequency spectrum is dominated by ultra-low (<0.01 Hz) or high (>0.15 Hz) frequency; temporally, there were sudden jumps in the time course. Then these noise components were regressed out from the time courses. Spatial registration was conducted using the following procedure. First, EPI rs-fMRI images were co-registered to the anatomical RARE images from the same rat using "align_epi_anat.py" from AFNI (Glen et al. 2020). Second, the T2-weighted images of all subjects were averaged to generate a rat brain template. Then, this template was registered to the SIGMA rat brain template (Barriere et al. 2019). Third, after denoising these components, fMRI data from each rat in the first step were aligned to the SIGMA rat brain templates using the co-registration parameters obtained previously. The SIGMA atlases (Barriere et al. 2019) were used to define seeds and different regions for the seed-based analysis. Posterior cingulate cortex and lateral EC were selected as seeds to correlate the whole-brain fMRI in Figs 4(d) and 5, respectively.
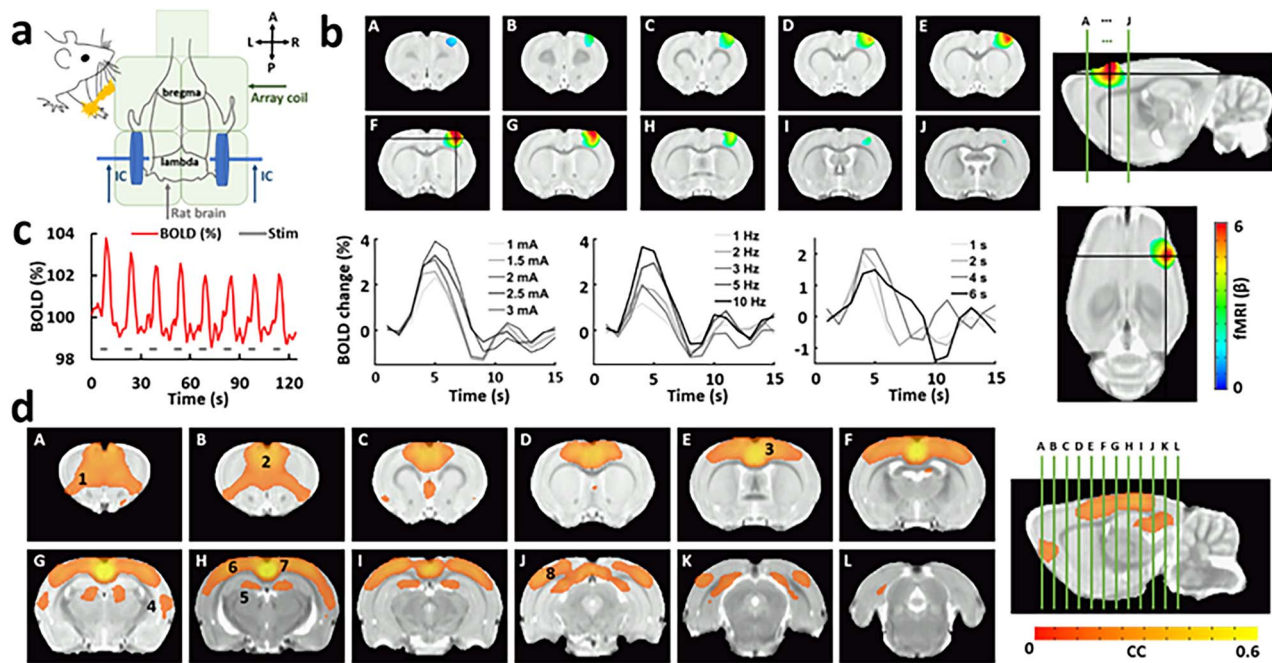
Fig. 4. BOLD fMRI responses induced with left forepaw electrical stimulation and DMN rs-fMRI functional connectivity in dementia rats. (a) 2D schematic of bilateral ICE placement (blue arrows). (b) Evoked BOLD fMRI maps show activation in S1FL following tactile stimulation of the left forepaw ($n = 5$ animals). GLM-based t-statistics in AFNI are used. P (corrected) < 0.001. (c) (Left) Averaged tracing of S1FL BOLD signal evolution over the time course upon forepaw stimulation ($n = 5$ animals). (Right) Mean BOLD signal alterations from a representative rat following various stimulation intensities (1, 1.5, 2, 2.5, 3 mA, 3 Hz, 4 s, 333 μs pulse width), frequencies (1, 2, 3, 5, 10 Hz, 2 mA, 4 s, 333 μs pulse width), and durations (1, 2, 4, 6 s, 3 Hz, 2 mA, 333 μs pulse width). (d). Default-mode network (DMN) shown in color overly on the SIGMA rat brain atlas (Barriere et al. 2019), as constructed from the seed-based analysis of rs-fMRI data, with ICEs replacing conventional ear bars and with baby cream fulfilled in middle ears ($n = 5$ animals). Significant clusters include brain regions "1" (Orbitofrontal Cortex), "2" (Prelimbic Cortex), "3" (Anterior Cingulate Cortex), "4" (Auditory Cortex), "5" (Hippocampus), "6" (Posterior Parietal Cortex), "7" (Retrosplenial Cortex) and "8" (Visual Cortex V1/V2).
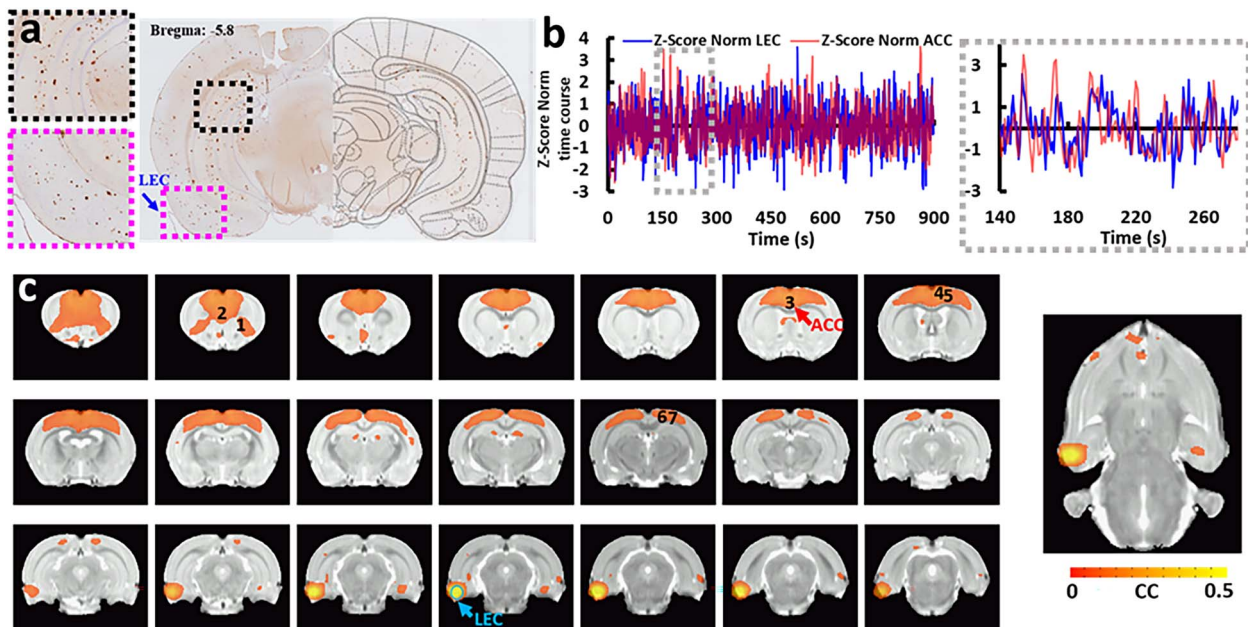
Fig. 5. Left lateral EC-based whole-brain connectivity. (a) Amyloid-β deposition with antibodies in the brain slice and anatomical location of the EC in a representative rat. (b) Normalized time courses from two highly correlated regions from a representative rat, left lateral EC as seed region with ICEs in place, as the blue arrow shows the ROI in (c) and ACC (red line), as the red arrow shows the ROI in (d). (c) Left lateral EC-based rs-fMRI connectivity maps show the local connectivity in the EC region and amygdala hippocampal area in a mixed dementia rat model ($n = 5$ animals). The correlation maps indicate strong connectivity to "1" Prefrontal Cortex, "2" Prelimbic Cortex, "3" Anterior Cingulated Cortex, "4" Secondary Motor Cortex, "5" Primary Motor Cortex, "6" Medio Medial Secondary Visual Cortex, and "7" Medio Lateral Secondary Visual Cortex based on SIGMA rat brain atlas (Barriere et al. 2019).

To compare the image sensitivity in enhanced versus unenhanced regions, we calculated SNR according to the following formula:

$$SNR_j = \frac{\overline{SI_j}}{\sigma_{background}}$$

where $\overline{SI_j}$ stands for the average signal intensity in the ROIs labeled by j, indicating enhanced or unenhanced regions, and $\sigma_{background}$ stands for the standard deviation of background signal intensity in the difference image.

Results

Design, characterization, and ex vivo evaluation of the ICEs

To evaluate the sensitivity enhancement capability of the ICE, we first acquired control images using a phased array coil placed above a 21-mm water tube that was secured inside the cradle by ear bars from the contralateral sides (Fig. 1a). We repeated the image acquisition twice and calculated the SNR map (Fig. 1b,c,h) by dividing the average signal intensity of each voxel with the standard deviation of background signal intensity in the different images. Then, we replaced the left ear bar with the ICE and pressed its flange surface against the outer surface of the glass tube. Based on this detection configuration, we acquired another set of images using the same parameters and calculated the SNR map again (Fig. 1c, f, i). Owing to effective inductive coupling, the ICE can "attract" the B1 field into the circular plane and concentrate magnetic flux, leading to focal sensitivity enhancement. This signal enhancement capability was visualized by the calculated ratio between the SNR maps obtained in the presence and absence of ICE (i.e. *Enhancement ratio* $= SNR_{ICE}/SNR_{No\ ICE}$). As shown in Fig. 1(d, g, j), the ICE can enhance detection sensitivity by > 2-fold for regions up to 2 mm away from the sample tube's surface. For a distance separated up to 5 mm from the surface, the ICE can gain at least 20% improvement in detection sensitivity. This effective range is more than enough to cover the EC area in brain limbic regions when the ICE is pressed against the rat's ear.

In vivo evaluation of baby cream and ICEs with restored BOLD fMRI mapping in rat brains

After applying baby cream in the ears (Fig. 2a, more detailed procedure in Methods and Movie S1), ICE was evaluated in vivo to measure enhanced MRI signal in the left (Fig. 2) or right (Fig.S1) hemisphere. First, introduction of the baby cream through a blunt tubing puncture into the middle ear allows restoration of GE-EPI signal loss induced by magnetic susceptibility mismatch (Fig. 2a). Because the baby cream is solid inside the ear, no plug was needed to keep it from leaking out, thus simplifying experimental procedures. The baby cream was used to fill the right middle ear cavity and ear canal, but none was used in the left ear. Compared to the restored EPI signals in the right hemisphere, part of the lateral hypothalamus, most of the EC, and the entire amygdala in the left hemisphere are affected by the susceptibility artifacts (Fig. 2b, c). Figure 2(d) shows representative EPI images (upper row, parameters in Methods) and RARE images (lower row, parameters in Methods). As expected, the signal restoration in the EPI images shows negligible influence on anatomical RARE images (Fig. 2e). Noteworthily, both tympanic membranes (eardrum; myringa) were penetrated when the baby cream was injected into the middle cavity and ear canal in both ears, and thus led to minimal auditory responses due to the MRI scanner acoustic noise. The damage of tympanic membranes will limit applications in some chronic studies.

Next, a 9-mm single loop ICE was used to replace the left ear bar beneath the Bruker commercial surface coil array to compare the SNR of deep regions in two hemispheres (Fig. 3a). By relaying locally detected MR signals to the external coil array, the ICE can enlarge the effective detection area on the left hemisphere and homogenize the image intensity between the bottom and top parts of the left cortex, leading to focal intensity enhancement in the left EC, as observed in the anatomical RARE MR images (Fig. 3b, yellow arrows). In contrast, because the ICE is absent on the right side, the top part of the right cortex remains to have higher intensity than the bottom part. It is noteworthy that no modifications to the scanner signal interface were required. The focal signal intensity in ROI 1 with the ICE in the left hemisphere was significantly higher than that of ROI 2 in the right hemisphere without ICE (Fig. 3b, c), and vice versa when the right ear bar was replaced by the ICE (Fig. S1a). It is noteworthy that the ICE could cover a large width along the anterior-posterior direction (particularly for paraflocculus in the cerebellum, Fig. S1b) and the ventral-dorsal direction (Fig. S2). This setup allows enhanced fMRI image signals for restored functional connectivity in rat brains.

Evaluation of the feasibility of ICE at the fMRI platform with tasked and rs-fMRI

After replacing the ear bars with two ICEs, we next tested the complexity and stability for animal experiments by measuring whole-brain fMRI signal with electrical stimulation on the left forepaw and then rs-fMRI connectivity in anesthetized rats (Fig. 4). The brain activation pattern upon left forepaw electrical stimulation is presented in Fig. 4(b), showing robust BOLD fMRI signals in the forelimb area of the primary somatosensory cortex of (S1FL). Figure 4(c) shows the temporal evolution of the BOLD signals in the S1FL with the averaged time courses acquired at different stimulation intensities, pulse frequencies, and pulse durations. Functional patterns obtained under various stimulation parameters are demonstrated in Figs S3 and S4(a). It is also noteworthy that ICEs ensure highly comparable activation patterns across different animals as shown in results from five individual rats (Figs S3 and S4a). Figure S4(b) shows activation in the S2 and S1FL in the other hemispheres from two representative rats. With respect to rs-fMRI, seed-based connectivity analysis of the DMN was conducted, following ICA to denoise the fMRI data (Fig. S5, details in Methods) and alignment with the SIGMA rat brain atlas (Barriere et al. 2019). As shown in Fig. 4(d), highly correlated regions include the orbitofrontal cortex, prelimbic cortex, anterior cingulate cortex, auditory cortex, hippocampus, posterior parietal cortex, and retrosplenial cortex. Though these results did not demonstrate advantage of reduced susceptibility artifact nor increased sensitivity for task and DMN from rs-fMRI, these results are highly consistent with reports from other researchers (Lu et al. 2012; Hsu et al. 2016b; Tudela et al. 2019; Pradier et al. 2021; Jung et al. 2022; Lambers et al. 2022), providing strong evidence for highly reliable detection of BOLD fMRI signals under experimental conditions without any modification or complication of the experimental procedure.

Seed-based correlation map of the left lateral EC with ICE for AD animal studies

Grandjean and colleagues first reported optogenetics on excitatory neurons in EC-based whole brain task-fMRI in mice (Salvan et al. 2021; Mandino et al. 2022), but to the best of our knowledge, no studies have been performed in the resting state due to the

limited MRI sensitivity in the EC region. To demonstrate the capability of our novel ICEs in rs-fMRI studies, we analyzed the seed-based rs-fMRI connectivity maps of the left lateral EC in rats to generate the first reported lateral EC-based rs-fMRI study in rats. As shown in Fig. 5(a), the EC is located at the caudal end of the temporal lobe in rodents (Khan et al. 2014). Due to its diverse heterogeneous projections, we first confirmed and delineated the extent of amyloid-β deposition in brain slices from the rats used in this study. Figure 5(a) shows a representative coronal section and Fig. 5(b) demonstrates the highly correlated Z-score normalized time courses from the left lateral EC and the anterior cingulated cortex (ACC). Then we chose the region with prominent amyloid-β deposition as the seed to correlate the voxel-wise fMRI signals in a whole brain scale based on the SIGMA rat brain atlas (Barriere et al. 2019). Highly consistent with other studies (Vismer et al. 2015; Desikan et al. 2018), we observed correlations not only in the local EC region, Amygdala hippocampal Area (Fig. 5c), but also in Prefrontal Cortex, Prelimbic Cortex, ACC, Medio Lateral Secondary Visual Cortex, Medio Medial Secondary Visual Cortex, Primary Motor Cortex, and Secondary Motor Cortex (Fig. 5c). It is noteworthy that the connectivity to posterior cingulate cortex is not significantly strong (Fig. 5c and S6), this may result from the heterogeneous projections of EC to different subregions of cingulate cortex. These seed-based whole-brain connectivity patterns from the left lateral EC in rats warrant further studies on the dysfunction of the EC in AD for future studies.

Discussion

We developed the ICE in combination with the baby cream injection to increase fMRI detection sensitivity in deep brain regions and this strategy has several advantages for rodent brain research. First, it is noteworthy that the baby cream allows easier access and matching solidity to effectively reduce susceptibility artifacts. This feature is particularly desirable on a preclinical scanner whose limited bore size precludes the incorporation of extra hardware for localized shim coils (Hsu and Glover 2005; Stockmann et al. 2022). Compared to human scanners that have a larger number of artifact reduction protocols based on Z-shimming or RF pulse tailoring (Cho and Ro 1992; Stenger et al. 2000; Yip et al. 2006), the pulse sequences available on a pre-clinical scanner are relatively basic, making our baby cream strategy desirable to implement. A simple injection of baby cream into the ear canal can already enable connectivity mapping across most brain regions, including deep brain regions such as EC and amygdala (Campolongo et al. 2009). Second, the BOLD fMRI with lower structure contrast and spatial resolution are registered to the high-resolution anatomical images for group analysis. With the signal dropout restored by ICE and baby cream, the whole-brain boundary could be used as a landmark to co-register activation maps (Sydekum et al. 2009). This is particularly helpful to keep signals after averaging in the small nuclei that are affected dramatically by the quality of image registration. Without this highly desirable feature, image registration becomes less accurate. Finally, as shown in Fig. 3(b) and Fig. S2, the ICE could increase the SNR across a range of brain regions, notably, without any modification of the MRI scanner interface or complication of the experimental setup. When the ICE is applied to various transgenic AD rodent lines (Sturchler-Pierrat et al. 1997; Wiesmann et al. 2017; Dawson et al. 2018; Gotz et al. 2018; Baglietto-Vargas et al. 2021), it will provide a highly promising imaging platform for fMRI studies in both healthy and diseased animal models.

Extensive studies have revealed the critical role that EC plays in AD, while functional characterization of EC has been limited by the lack of effective imaging modalities for in vivo whole-brain imaging with high SNR in deep brain regions. Functional ultrasound is an emerging promising tool with proper sensitivity and resolution, but when taking into consideration the in vivo whole-brain, non-invasive, and translational value of fMRI, there is still a need and value to optimize the fMRI method. However, due to the long distance separating deep brain regions and the surface coil placed above the skull, as well as susceptibility artifacts induced by the air in the ear cavity, it remains extremely challenging to study the functional role the EC plays in AD using fMRI. The EC is less explored in both patients and AD animal models compared to the widely investigated DMN hubs (Schwindt et al. 2013; Zhu et al. 2013; Grieder et al. 2018; Rauchmann et al. 2021) in cortex or subcortical regions, e.g. hippocampus. From a structural perspective with MRI anatomical imaging, Jessen and colleagues reported a mean EC volume reduction of 18% in patients with subjective memory impairment, 26% in patients with mild cognitive impairment, and 44% in patients with AD (Jessen et al. 2006). From the molecular perspective, Khan and colleagues have found that the lateral EC was particularly sensitive to tau and amyloid pathology and that lateral EC dysfunction could spread to the parietal cortex (Khan et al. 2014) and, recently, it was shown that EC layer II contains reelin-positive projection neurons, underscoring the established linkage between reelin dysfunction and plaque and tangle pathologies (Kobro et al. 2021). The imaging scheme of ICE with baby cream makes it possible to establish EC-based connectivity in animals (Fig. 5), bringing a missing piece to study the EC-mediated whole-brain connectivity in AD rodent models. More detailed analysis for in-depth EC activity and connectivity in different animal groups are underway, which will be reported in our future work. Our methodology may provide new insights into different EC connectivity patterns in healthy and AD animals, enabling us to search for novel preclinical fMRI biomarkers for AD.

Several limitations about the usage of ICE should be considered when interpreting the results of this study and for future optimization of the ICE for animal fMRI. First, the ICE increases focal sensitivity by "attracting" magnetic flux through its circular plane, thus redistributing B1 across the entire sample. This also means the focal sensitivity is increased near the ICE but at the cost of sensitivity decreases in regions far away from the ICE. For example, when the ICE is placed against the bottom left surface of the sample (e.g. in Figs. 1c and 3b), signal intensities in the left hemisphere become comparable between the lower and the upper regions while the right hemisphere has higher intensity only in its upper part. However, the limited FOV of an individual ICE can be overcome by incorporating another ICE on the right side to increase the coverage area, enabling sensitivity gain on both sides of the sample. To ensure sensitivity enhancement for a certain detection depth, we need to adjust the diameter of ICE to approximately twice the desired detection depth. Based on our empirical experience with rats with body weight 200–400 g, the current ICE design with a diameter of 9 mm has a larger brain parenchyma coverage with the signal enhancement in the smaller rats (Fig. 1). We anticipate that for a larger rat with a long distance between the brain parenchyma and the skin, the size of ICE would be scaled proportionally to keep a similar level of SNR enhancement over a conventional surface array. Similarly, for mouse studies, it will be necessary to re-design a smaller ICE with matching geometrical parameters. This is undergoing with our current project, which is to fabricate an inductively coupled detector that could both increase SNR for MR imaging and also

be applied for mice studies. Second, because the materials used for the 3D printing are UV-curable photopolymer, they could not be as stiff as the ear bars made of carbon fiber. Therefore, for awake animal studies, there is still room for improvement from the material perspective for the inductively coupled ear bars. It is also worth pointing out that in rare occasions if a rat wakes up during scanning and struggles violently, the ICE can be bent and broken. In addition, due to difficulties in applying baby cream to awake animals, the application of this study remains limited in awake fMRI studies (Gao et al. 2017; Desjardins et al. 2019; Tsurugizawa et al. 2020; Gutierrez-Barragan et al. 2022; Zeng et al. 2022). Thus, measurements were performed only under a well-controlled anesthetic condition. Third, once the tympanic membranes are penetrated, the baby cream in the ear cavity is difficult to completely remove after experiments. The residual cream could attenuate the acoustic effect induced by EPI gradient switching sounds but may affect animal behaviors. Pain medication after penetration of the tympanic membrane should be applied in unanesthetized animals. For application scenarios when ear-filling is not desirable (e.g. in longitudinal studies) the ICE itself can still improve detection sensitivity for brain regions near the ear cavity because these regions are vulnerable to susceptibility artifacts. Moreover, if preclinical scanners can eventually have access to the more sophisticated techniques that are only available on clinical scanners, such as Z-shimming or RF pulse tailoring (Cho and 1992; Stenger et al. 2000; Yip et al. 2006) without the using of the baby cream to fill the ear cavities, the ICE can further improve their performance. All these effects should be taken into consideration, therefore limiting this methodology for longitudinal studies. Lastly, although the ICE has a 2-fold and obvious SNR enhancement in regions adjacent to the skull, such as the EC and the paraflocculus in the cerebellum, its passive coupling limits the effective enhancement depth, leading to no SNR improvement in regions farther away from the skull, such as the lateral hypothalamus, ventral tegmental area, etc. In the future, it will be worthwhile to explore the Wirelessly Amplified NMR Detector (Qian et al. 2013) with the ear bar to actively amplify MRI signals, leading to improved effective detection range with an additional > 3-fold sensitivity gains over the passive coupling in deeper brain regions.

Conclusions

In summary, we have implemented novel ICEs in the 7 T scanner to yield high-resolution structural and functional images of the rat brain by reducing susceptibility-induced signal loss in functional MRI. The ICE-based mapping scheme enables EC-driven brain connectivity studies with a simplified experimental setup, providing opportunities to further study EC in AD animal models using fMRI coupled with additional modalities such as optogenetics and calcium recordings. This setup could also be applied in other deep brain fMRI studies suffering from susceptibility artifacts in both healthy and diseased rodent studies.

CRediT statement

Yi Chen (Conceptualization, Data curation, Investigation, Methodology, Validation, Writing—original draft), Zachary Fernandez (Investigation), Norman Scheel (Data curation), Mahsa Gifani (Resources), David Zhu (Methodology, Resources), Scott Counts (Investigation, Resources), Ann Dorrance (Resources), Daniel Razansky (Writing—review and editing), Xin Yu (Conceptualization), Wei Qian (Data curation), Chunqi Qian (Conceptualization, Data curation, Formal analysis, Funding acquisition, Investigation, Methodology, Project administration, Resources, Supervision, Validation, Writing—review and editing).

Supplementary material

Supplementary material is available at *Cerebral Cortex* online.

Funding

Data availability

The data supporting this study's findings are available from the following site: https://openneuro.org/datasets/ds004797.

Code availability

The related image processing codes are available from the following site https://openneuro.org/datasets/ds004797.

References

Baglietto-Vargas D, Forner S, Cai L, Martini AC, Trujillo-Estrada L, Swarup V, Nguyen MMT, Do Huynh K, Javonillo DI, Tran KM, et al. Generation of a humanized Abeta expressing mouse demonstrating aspects of Alzheimer's disease-like pathology. *Nat Commun*. 2021:12:2421.

Barriere DA, Magalhaes R, Novais A, Marques P, Selingue E, Geffroy F, Marques F, Cerqueira J, Sousa JC, Boumezbeur F, et al. The SIGMA rat brain templates and atlases for multimodal MRI data analysis and visualization. *Nat Commun*. 2019:10:5699.

Biswal B, Yetkin FZ, Haughton VM, Hyde JS. Functional connectivity in the motor cortex of resting human brain using echo-planar MRI. *Magnet Reson Med*. 1995:34:537–541.

Brun VH, Leutgeb S, Wu HQ, Schwarcz R, Witter MP, Moser EI, Moser MB. Impaired spatial representation in CA1 after lesion of direct input from entorhinal cortex. *Neuron*. 2008:57:290–302.

Campolongo P, Roozendaal B, Trezza V, Hauer D, Schelling G, McGaugh JL, Cuomo V. Endocannabinoids in the rat basolateral amygdala enhance memory consolidation and enable glucocorticoid modulation of memory. *Proc Natl Acad Sci U S A*. 2009:106: 4888–4893.

Chavoshinezhad S, Zibaii MI, Seyed Nazari MH, Ronaghi A, Asgari Taei A, Ghorbani A, Pandamooz S, Salehi MS, Valian N, Motamedi F, et al. Optogenetic stimulation of entorhinal cortex reveals the implication of insulin signaling in adult rat's hippocampal neurogenesis. *Prog Neuro-Psychopharmacol Biol Psychiatry*. 2021:111:110344.

Chen Y, Sobczak F, Pais-Roldan P, Schwarz C, Koretsky AP, Yu X. Mapping the brain-wide network effects by optogenetic activation of the corpus callosum. *Cereb Cortex*. 2020:30:5885–5898.

Chen Y, Wang Q, Choi S, Zeng H, Takahashi K, Qian CQ, Yu X. Focal fMRI signal enhancement with implantable inductively coupled detectors. *NeuroImage*. 2022:247:118793.

Cho ZH, Ro YM. Reduction of susceptibility artifact in gradient-echo imaging. *Magn Reson Med*. 1992:23:193–200.

Chuang KH, Lee HL, Li Z, Chang WT, Nasrallah FA, Yeow LY, Singh K. Evaluation of nuisance removal for functional MRI of rodent brain. *NeuroImage*. 2019:188:694–709.

Cohen RM, Rezai-Zadeh K, Weitz TM, Rentsendorj A, Gate D, Spivak I, Bholat Y, Vasilevko V, Glabe CG, Breunig JJ, et al. A transgenic Alzheimer rat with plaques, Tau pathology, behavioral impairment, oligomeric Abeta, and frank neuronal loss. *J Neurosci*. 2013:33:6245–6256.

Dawson TM, Golde TE, Lagier-Tourenne C. Animal models of neurodegenerative diseases. *Nat Neurosci*. 2018:21:1370–1379.

Desikan S, Koser DE, Neitz A, Monyer H. Target selectivity of septal cholinergic neurons in the medial and lateral entorhinal cortex. *P Natl Acad Sci USA*. 2018:115:E2644–E2652.

Desjardins M, Kilic K, Thunemann M, Mateo C, Holland D, Ferri CGL, Cremonesi JA, Li B, Cheng Q, Weldy KL, et al. Awake mouse imaging: from two-photon microscopy to blood oxygen level-dependent functional magnetic resonance imaging. *Biol Psychiatry Cogn Neurosci Neuroimaging*. 2019:4:533–542.

Farahani K, Sinha U, Sinha S, Chiu LC, Lufkin RB. Effect of field strength on susceptibility artifacts in magnetic resonance imaging. *Comput Med Imaging Graph*. 1990:14:409–413.

Fyhn M, Molden S, Witter MP, Moser EI, Moser MB. Spatial representation in the entorhinal cortex. *Science*. 2004:305: 1258–1264.

Gao YR, Ma Y, Zhang Q, Winder AT, Liang Z, Antinori L, Drew PJ, Zhang N. Time to wake up: studying neurovascular coupling and brain-wide circuit function in the un-anesthetized animal. *NeuroImage*. 2017:153:382–398.

Glen DR, Taylor PA, Buchsbaum BR, Cox RW, Reynolds RC. Beware (surprisingly common) left-right flips in your MRI data: an efficient and robust method to check MRI dataset consistency using AFNI. *Front Neuroinform*. 2020:14:18.

Gotz J, Bodea LG, Goedert M. Rodent models for Alzheimer disease. *Nat Rev Neurosci*. 2018:19:583–598.

Grieder M, Wang DJJ, Dierks T, Wahlund LO, Jann K. Default mode network complexity and cognitive decline in mild Alzheimer's disease. *Front Neurosci*. 2018:12:770.

Griffanti L, Salimi-Khorshidi G, Beckmann CF, Auerbach EJ, Douaud G, Sexton CE, Zsoldos E, Ebmeier KP, Filippini N, Mackay CE, et al. ICA-based artefact removal and accelerated fMRI acquisition for improved resting state network imaging. *NeuroImage*. 2014:95: 232–247.

Griffanti L, Douaud G, Bijsterbosch J, Evangelisti S, Alfaro-Almagro F, Glasser MF, Duff EP, Fitzgibbon S, Westphal R, Carone D, et al. Hand classification of fMRI ICA noise components. *NeuroImage*. 2017:154:188–205.

Gutierrez-Barragan D, Singh NA, Alvino FG, Coletta L, Rocchi F, De Guzman E, Galbusera A, Uboldi M, Panzeri S, Gozzi A. Unique spatiotemporal fMRI dynamics in the awake mouse brain. *Curr Biol*. 2022:32:631–644 e636.

Hernandez CM, Orsini CA, Labiste CC, Wheeler AR, Ten Eyck TW, Bruner MM, Sahagian TJ, Harden SW, Frazier CJ, Setlow B, et al. Optogenetic dissection of basolateral amygdala contributions to intertemporal choice in young and aged rats. *Elife*. 2019:8:e46174.

Hsu JJ, Glover GH. Mitigation of susceptibility-induced signal loss in neuroimaging using localized shim coils. *Magn Reson Med*. 2005:53:243–248.

Hsu LM, Liang X, Gu H, Brynildsen JK, Stark JA, Ash JA, Lin CP, Lu H, Rapp PR, Stein EA, et al. Constituents and functional implications of the rat default mode network. *Proc Natl Acad Sci U S A*. 2016a:113:E4541–E4547.

Hsu LM, Liang X, Gu H, Brynildsen JK, Stark JA, Ash JA, Lin CP, Lu HB, Rapp PR, Stein EA, et al. Constituents and functional implications of the rat default mode network. *Proc Natl Acad Sci U S A*. 2016b:113:E4541–E4547.

Jacobs J, Miller J, Lee SA, Coffey T, Watrous AJ, Sperling MR, Sharan A, Worrell G, Berry B, Lega B, et al. Direct electrical stimulation of the human entorhinal region and hippocampus impairs memory. *Neuron*. 2016:92:983–990.

Jessen F, Feyen L, Freymann K, Tepest R, Maier W, Heun R, Schild HH, Scheef L. Volume reduction of the entorhinal cortex in subjective memory impairment. *Neurobiol Aging*. 2006:27:1751–1756.

Jung WB, Jiang H, Lee S, Kim SG. Dissection of brain-wide resting-state and functional somatosensory circuits by fMRI with optogenetic silencing. *Proc Natl Acad Sci U S A*. 2022:119(4):e2113313119.

Kelly SC, McKay EC, Beck JS, Collier TJ, Dorrance AM, Counts SE. Locus coeruleus degeneration induces forebrain vascular pathology in a transgenic rat model of Alzheimer's disease. *J Alzheimers Dis*. 2019:70:371–388.

Khan UA, Liu L, Provenzano FA, Berman DE, Profaci CP, Sloan R, Mayeux R, Duff KE, Small SA. Molecular drivers and cortical spread of lateral entorhinal cortex dysfunction in preclinical Alzheimer's disease. *Nat Neurosci*. 2014:17:304–311.

Kobro-Flatmoen A, Lagartos-Donate MJ, Aman Y, Edison P, Witter MP, Fang EF. Re-emphasizing early Alzheimer's disease pathology starting in select entorhinal neurons, with a special focus on mitophagy. *Ageing Res Rev*. 2021:67:101307.

Lambers H, Wachsmuth L, Thomas D, Boumezbeur F, Hoesker V, Pradier B, Faber C. Fiber-based lactate recordings with fluorescence resonance energy transfer sensors by applying an magnetic resonance-informed correction of hemodynamic artifacts. *Neurophotonics*. 2022:9:032212.

Lee JH, Durand R, Gradinaru V, Zhang F, Goshen I, Kim DS, Fenno LE, Ramakrishnan C, Deisseroth K. Global and local fMRI signals driven by neurons defined optogenetically by type and wiring. *Nature*. 2010:465:788–792.

Lee HL, Li Z, Coulson EJ, Chuang KH. Ultrafast fMRI of the rodent brain using simultaneous multi-slice EPI. *NeuroImage*. 2019:195: 48–58.

Lee JY, You T, Lee CH, Im GH, Seo H, Woo CW, Kim SG. Role of anterior cingulate cortex inputs to periaqueductal gray for pain avoidance. *Curr Biol*. 2022:32:2834–2847 e2835.

Li RP, Liu XP, Sidabras JW, Paulson ES, Jesmanowicz A, Nencka AS, Hudetz AG, Hyde JS. Restoring susceptibility induced MRI signal loss in rat brain at 9.4 T: a step towards whole brain functional connectivity imaging. *PLoS One*. 2015:10(4):e0119450.

Liu Y, Perez PD, Ma Z, Ma Z, Dopfel D, Cramer S, Tu W, Zhang N. An open database of resting-state fMRI in awake rats. *NeuroImage*. 2020:220:117094.

Logothetis NK. What we can do and what we cannot do with fMRI. *Nature*. 2008:453:869–878.

Lu HB, Zou QH, Gu H, Raichle ME, Stein EA, Yang YH. Rat brains also have a default mode network. *Proc Natl Acad Sci U S A*. 2012:109: 3979–3984.

Lu Y, Zhong C, Wang L, Wei P, He W, Huang K, Zhang Y, Zhan Y, Feng G, Wang L. Optogenetic dissection of ictal propagation

in the hippocampal-entorhinal cortex structures. *Nat Commun.* 2016:7:10962.

Lv H, Wang Z, Tong E, Williams LM, Zaharchuk G, Zeineh M, Goldstein-Piekarski AN, Ball TM, Liao C, Wintermark M. Resting-state functional MRI: everything that nonexperts have always wanted to know. *Am J Neuroradiol.* 2018:39:1390–1399.

Mahesh M. The essential physics of medical imaging, third edition. *Med Phys.* 2013:40(7):077301.

Mandeville JB, Marota JJA, Kosofsky BE, Keltner JR, Weissleder R, Rosen BR, Weisskoff RM. Dynamic functional imaging of relative cerebral blood volume during rat forepaw stimulation. *Magnet Reson Med.* 1998:39:615–624.

Mandino F, Yeow LY, Bi RZ, Sejin L, Bae HG, Baek SH, Lee CY, Mohammad H, Horien C, Teoh CL, et al. The lateral entorhinal cortex is a hub for local and global dysfunction in early Alzheimer's disease states. *J Cerebr Blood F Met.* 2022:42:1616–1631.

Mankin EA, Fried I. Modulation of human memory by deep brain stimulation of the entorhinal-hippocampal circuitry. *Neuron.* 2020:106:218–235.

Matin N, Fisher C, Lansdell TA, Hammock BD, Yang J, Jackson WF, Dorrance AM. Soluble epoxide hydrolase inhibition improves cognitive function and parenchymal artery dilation in a hypertensive model of chronic cerebral hypoperfusion. *Microcirculation.* 2021:28:e12653.

Mechling AE, Arefin T, Lee HL, Bienert T, Reisert M, Ben Hamida S, Darcq E, Ehrlich A, Gaveriaux-Ruff C, Parent MJ, et al. Deletion of the mu opioid receptor gene in mice reshapes the reward-aversion connectome. *Proc Natl Acad Sci U S A.* 2016:113:11603–11608.

Nasrallah FA, To XV, Chen DY, Routtenberg A, Chuang KH. Functional connectivity MRI tracks memory networks after maze learning in rodents. *NeuroImage.* 2016:127:196–202.

Pires PW, Jackson WF, Dorrance AM. Regulation of myogenic tone and structure of parenchymal arterioles by hypertension and the mineralocorticoid receptor. *Am J Physiol Heart Circ Physiol.* 2015:309:H127–H136.

Pradier B, Wachsmuth L, Nagelmann N, Segelcke D, Kreitz S, Hess A, Pogatzki-Zahn EM, Faber C. Combined resting state-fMRI and calcium recordings show stable brain states for task-induced fMRI in mice under combined ISO/MED anesthesia. *NeuroImage.* 2021:245:118626.

Qian C, Yu X, Chen D, Dodd S, Bouraoud N, Pothayee N, Chen Y, Beeman S, Bennett K, Murphy-Boesch J, et al. Wireless Amplified NMR Detector (WAND) for high resolution MRI of internal organs: preclinical demonstration in a rodent model. *Radiology.* 2013:268:228–236.

Rauchmann BS, Ersoezlue E, Stoecklein S, Keeser D, Brosseron F, Buerger K, Dechent P, Dobisch L, Ertl-Wagner B, Fliessbach K, et al. Resting-state network alterations differ between Alzheimer's disease atrophy subtypes. *Cereb Cortex.* 2021:31:4901–4915.

Ryu JK, Jung WB, Yu J, Son JP, Lee SK, Kim SG, Park JY. An equal-TE ultrafast 3D gradient-echo imaging method with high tolerance to magnetic susceptibility artifacts: application to BOLD functional MRI. *Magn Reson Med.* 2021:85:1986–2000.

Salvan P, Lazari A, Vidaurre D, Mandino F, Johansen-Berg H, Grandjean J. Frequency modulation of entorhinal cortex neuronal activity drives distinct frequency-dependent states of brain-wide dynamics. *Cell Rep.* 2021:37:109954.

Schnall MD, Barlow C, Subramanian VH, Leigh JS. Wireless implanted magnetic-resonance probes for invivo NMR. *J Magn Reson.* 1986:68:161–167.

Schwindt GC, Chaudhary S, Crane D, Ganda A, Masellis M, Grady CL, Stefanovic B, Black SE. Modulation of the default-mode network between rest and task in Alzheimer's disease. *Cereb Cortex.* 2013:23:1685–1694.

Stenger VA, Boada FE, Noll DC. Three-dimensional tailored RF pulses for the reduction of susceptibility artifacts in T($*$)(2)-weighted functional MRI. *Magn Reson Med.* 2000:44:525–531.

Stockmann JP, Arango NS, Witzel T, Mareyam A, Sappo C, Zhou J, Jenkins L, Craven-Brightman L, Milshteyn E, Davids M, et al. A 31-channel integrated "AC/DC" B(0) shim and radiofrequency receive array coil for improved 7T MRI. *Magn Reson Med.* 2022:87:1074–1092.

Sturchler-Pierrat C, Abramowski D, Duke M, Wiederhold KH, Mistl C, Rothacher S, Ledermann B, Burki K, Frey P, Paganetti PA, et al. Two amyloid precursor protein transgenic mouse models with Alzheimer disease-like pathology. *Proc Natl Acad Sci U S A.* 1997:94:13287–13292.

Suthana N, Haneef Z, Stern J, Mukamel R, Behnke E, Knowlton B, Fried I. Memory enhancement and deep-brain stimulation of the entorhinal area. *N Engl J Med.* 2012:366:502–510.

Sydekum E, Baltes C, Ghosh A, Mueggler T, Schwab ME, Rudin M. Functional reorganization in rat somatosensory cortex assessed by fMRI: elastic image registration based on structural landmarks in fMRI images and application to spinal cord injured rats. *NeuroImage.* 2009:44:1345–1354.

Tsao A, Sugar J, Lu L, Wang C, Knierim JJ, Moser MB, Moser EI. Integrating time from experience in the lateral entorhinal cortex. *Nature.* 2018:561:57–62.

Tsoi SY, Oncul M, Svahn E, Robertson M, Bogdanowicz Z, McClure C, Surmeli G. Telencephalic outputs from the medial entorhinal cortex are copied directly to the hippocampus. *Elife.* 2022:11:e73162.

Tsurugizawa T, Tamada K, Ono N, Karakawa S, Kodama Y, Debacker C, Hata J, Okano H, Kitamura A, Zalesky A, et al. Awake functional MRI detects neural circuit dysfunction in a mouse model of autism. *Sci Adv.* 2020:6:eaav4520.

Tudela R, Munoz-Moreno E, Sala-Llonch R, Lopez-Gil X, Soria G. Resting state networks in the TgF344-AD rat model of Alzheimer's disease are altered from early stages. *Front Aging Neurosci.* 2019:11:213.

Vismer MS, Forcelli PA, Skopin MD, Gale K, Koubeissi MZ. The piriform, perirhinal, and entorhinal cortex in seizure generation. *Front Neural Circuit.* 2015:9:27.

Wiesmann M, Roelofs M, van der Lugt R, Heerschap A, Kiliaan AJ, Claassen JA. Angiotensin II, hypertension and angiotensin II receptor antagonism: roles in the behavioural and brain pathology of a mouse model of Alzheimer's disease. *J Cereb Blood Flow Metab.* 2017:37:2396–2413.

Wirth ED, Mareci TH, Beck BL, Fitzsimmons JR, Reier PJ. A comparison of an inductively-coupled implanted coil with optimized surface coils for in-vivo NMR imaging of the spinal-cord. *Magnet Reson Med.* 1993:30:626–633.

Witter MP, Moser EI. Spatial representation and the architecture of the entorhinal cortex. *Trends Neurosci.* 2006:29:671–678.

Xia F, Yiu A, Stone SSD, Oh S, Lozano AM, Josselyn SA, Frankland PW. Entorhinal cortical deep brain stimulation rescues memory deficits in both young and old mice genetically engineered to model Alzheimer's disease. *Neuropsychopharmacology.* 2017:42:2493–2503.

Yamori Y, Horie R, Handa H, Sato M, Okamoto K. Proceedings: studies on stroke in stroke-prone spontaneously hypertensive rats (SHRSP). (I). Local factor analysis on stroke. *Jpn Heart J.* 1975:16:329–331.

Yip CY, Fessler JA, Noll DC. Advanced three-dimensional tailored RF pulse for signal recovery in T2∗-weighted functional magnetic resonance imaging. *Magn Reson Med*. 2006:56:1050–1059.

Yoo S, Song H, Kim SG, Shim WM, Lee SK. Feasibility of head-tilted brain scan to reduce susceptibility-induced signal loss in the prefrontal cortex in gradient echo-based imaging. *NeuroImage*. 2020:223:117265.

Zeng H, Jiang Y, Beer-Hammer S, Yu X. Awake mouse fMRI and pupillary recordings in the ultra-high magnetic field. *Front Neurosci*. 2022:16:886709.

Zerbi V, Grandjean J, Rudin M, Wenderoth N. Mapping the mouse brain with rs-fMRI: an optimized pipeline for functional network identification. *NeuroImage*. 2015:123:11–21.

Zhang SJ, Ye J, Miao C, Tsao A, Cerniauskas I, Ledergerber D, Moser MB, Moser EI. Optogenetic dissection of entorhinal-hippocampal functional connectivity. *Science*. 2013:340:1232627.

Zhu DC, Majumdar S, Korolev IO, Berger KL, Bozoki AC. Alzheimer's disease and amnestic mild cognitive impairment weaken connections within the default-mode network: a multi-modal imaging study. *J Alzheimers Dis*. 2013:34:969–984.